Advances in Applied Mathematics and Mechanics
Adv. Appl. Math. Mech., Vol. **16**, No. 2, pp. 519-548

DOI: 10.4208/aamm.OA-2021-0326
April 2024

Investigating Droplet and Bubble Deformation under Shear Flow using the Multi-Pseudo-Potential Scheme of Lattice Boltzmann Method

Raheleh Sharifi[1], Mostafa Varmazyar[1,*] and Arash Mohammadi[1]

[1] *Department of Mechanical Engineering, Shahid Rajaee Teacher Training University, Shahid Shabanloo Ave., Tehran 16788-15811, Iran*

Received 25 October 2021; Accepted (in revised version) 19 April 2022

Abstract. In the present study, a multi-pseudo-potential model is used to simulate the deformation and breakup of bubbles and droplets under simple shear flow. It is shown that the current model can adjust the amount of surface tension, independent of the interface thickness, equation of state (EOS), and reduced temperature. Considering the available findings, no comprehensive study has been performed on all aspects of deformation of bubbles and droplets under shear flow using numerical methods. Bubble or droplet deformation under simple shear flow depends on two non-dimensional numbers: capillary number (Ca) and viscosity ratio (λ). In this investigation, various scenarios, including small deformation, large deformation, and breakup for bubbles $(0.2<\lambda<1)$ and droplets $(1<\lambda<5)$, are separately studied. Results of the multi-pseudo-potential model show that the bubble and droplet deformations oscillate under shear flow and undergo elongation and contraction over time to converge to the final shape. As the capillary increases by more than one, the bubble expands and shrinks. The bubble tips become sharp, and so-called slender, at a low viscosity ratio (λ). A detailed comparison is made between the numerical results for deformation parameters of the present model and the experimental results available in the references.

AMS subject classifications: 76T10, 76T06, 65Z99

Key words: Lattice Boltzmann method, multi-pseudo-potential scheme, droplet and bubble deformation, simple shear flow, capillary number.

1 Introduction

Multiphase flow is considered a continuum fluid flow with two different phases (i.e., gas and liquid) [1-3] and has particular importance in industrial and scientific applications [4]. Various numerical methods have been developed based on the macroscopic

---

[*]Corresponding author.
Email: varmazyar.mostafa@sru.ac.ir (M. Varmazyar)

approach, all of which require tracking the interface between the two phases in the flow simulation. However, the methods based on the mesoscopic approach, such as lattice Boltzmann method (LBM), can automatically detect the border of each phase without any extra calculations [5-7]. Besides, these methods do not require using the Poisson's equation for pressure correction. These specifications of the mesoscopic models make it possible to model two-phase flows with a more straightforward implementation algorithm and less computational cost than those for the conventional computational fluid dynamic schemes [8-10].

Color-gradient [11], Shan-Chen [12, 13], and free-energy [14, 15] are the three categories that have been introduced so far for the multiphase LBMs. Observations show that the Shan-Chen category has attracted more attention, which is due to the ease of implementation and robust description of particle interactions [3]. The main concern in using the Shan-Chen model is to achieve full thermodynamic consistency [16-18], meaning that energy conservation is maintained in the phase transition [16].

In the original Shan-Chen method, the interaction force between the particles is modeled by a pseudo-potential function (ψ). Numerous investigations have been performed on the relationship between pseudo-potential function and density of phases on the thermodynamic consistency [2, 3, 17, 19]. He and Doolen's [20] results demonstrated that the pseudo-potential function must be defined according to the density $(\psi \propto \rho)$ to achieve thermodynamic consistency. However, it is necessary to consider a suitable relationship between the pseudo-potential function and density in order to accurately calculate the pressure tensor [21]. Accordingly, Shan and Chen [13] demonstrated that $\psi = \psi_0 \exp -\rho_0/\rho$ could properly model pressure tensor. In another study, Sbragaglia et al. [22] showed that Shan's relation increased numerical instability and spurious velocities near the interface.

As mentioned earlier, the energy conservation must be satisfied in order to obtain a thermodynamically consistent model. Since the free energy method maintains this criterion, Sbragaglia and Shan tried to coincide the Shan-Chen model with the free energy method [23]. Their suggestion was to define a pseudo-potential function as $\psi = (\rho/(E+\rho))^{(1/E)}$, where E is a constant depending on the lattice [23, 24].

Various approaches have been taken to correct the shortcomings of the original Shan-Chen model, in all of which the idea of using a pseudo-potential function has been preserved. The results show this approach cannot take into account all the aspects related to intermolecular forces. Therefore, it cannot eliminate the thermodynamic inconsistency of the original Shan-Chen model [25, 26]. Accordingly, in the present study, a multi-pseudo-potential model is introduced to simulate two-phase flows. Each of the pseudo-potential functions is responsible for modeling a portion of the intermolecular forces. The suggestion of Sbragaglia and Shan has also been used to satisfy energy conservation. Khajepoor and Chen [17] represented that the multi-pseudo-potential scheme was utterly consistent with thermodynamics and could be used for engineering applications. Their results displayed this approach could reduce the spurious velocities in the interface of two phases. The multi-pseudo-potential Shan-Chen model can adjust the amount of surface tension, independent of the interface thickness, equation of state (EOS), and reduced temperature. Therefore, this model can be used for two-phase problems, in which the effects of surface tension cannot be ignored.

The problem of bubble (droplet) deformation in shear flow is selected to evaluate the abilities of the present model. The bubble (droplet) behavior in shear flow is investigated in three categories: small deformation, large deformation, and breakup [27-43]. The capillary number is far less or greater at small and large deformations than one ($Ca \ll 1$ and $Ca \gg 1$). In the present study, calculations are performed for the wide range of the capillary numbers ($0.05 < Ca < 8.0$).

In the next section, the multi-pseudo-potential Shan-Chen model is introduced. Then, details of the bubble (droplet) deformation problem in the shear flow are stated. First, the current multi-pseudo-potential Shan-Chen model is evaluated in flat interface and static droplet in the results section. Finally, the present results of the Shan-Chen model are compared with the experimental results reflected in previous experimental studies.

2 Multi-pseudo-potential Shan-Chen model

In this section, the multi-pseudo-potential Shan-Chen model is introduced.

2.1 Lattice Boltzmann equation

In the LBM, the microscopic particle behavior of fluid is modeled by the particle probability distribution function. The discrete lattice Boltzmann equation based on the Bhatnagar-Gross-Krook (BGK) approximation in the ith direction can be represented as follows [44]:

$$f_i(\mathbf{x}+\boldsymbol{e}_i\delta_t,t+\delta_t)-f_i(\mathbf{x},t)=-\frac{1}{\tau}\left[f_i(\mathbf{x},t)-f_i^{eq}(\mathbf{x},t)\right]+F_i(\mathbf{x},t), \tag{2.1}$$

where x and t are the location vector and time, respectively. τ is relaxation time, f_i is the one-particle velocity distribution function which travels with velocity e_i and F_i is the discrete form of intermolecular body force [45]. f_i^{eq} is the equilibrium distribution function, which can be defined as follows:

$$f_i^{eq}=\omega_i\rho\left(1+\frac{e_i\cdot u^{eq}}{c_s^2}+\frac{(e_i\cdot u^{eq})^2}{2c_s^4}-\frac{(u^{eq})^2}{2c_s^2}\right), \tag{2.2}$$

where ω_i are the weighting coefficients and $c_s=1/\sqrt{3}$ is the lattice sound. D2Q9 lattice is chosen for simulations. The weighting coefficients for this lattice are assumed by $\omega_i=4/9$ for $i=0$; $\omega_i=1/9$ for $i=1$–4, and $\omega_i=1/36$ for $i=5$–8. The discrete velocity vectors are defined as shown below:

$$e_i=\begin{cases}(0,0), & i=0,\\ (\pm1,0),(0,\pm1), & i=1-4,\\ (\pm1,\pm1), & i=5-8.\end{cases} \tag{2.3}$$

Using Chapman-Enskog analysis, the relationship between kinematic viscosity and relaxation time can be obtained as follows:

$$v = C_s^2\left(\tau - \frac{1}{2}\right)\delta_t. \tag{2.4}$$

The density and macroscopic velocity of the fluid can be calculated as shown below:

$$\rho = \sum_i f_i \quad \rho\vec{u} = \sum_i f_i e_i. \tag{2.5}$$

2.2 Multi-pseudo-potential scheme

Multi-pseudo-potentials are used to demonstrate the main interaction potentials in various extents of the mean free path of particles. This method can accurately model the cubic EOS. It can be proven that the multi-pseudo-potential scheme is consistent with thermodynamics [46]. The force term in this model can be defined as follows:

$$F_\mathrm{i}(\mathbf{x},t) = F^{(1)} + F^{(2)} + \cdots + F^{(n)} = \sum_{j=1}^{n} -G_j\psi_j(x,t)\sum_{i=1}^{N} w\left(|c_i|^2\right)\psi_j(x+c_i,t)c_i, \tag{2.6}$$

here pseudo-potential function $(\psi_j(x,t))$ is defined by Eq. (2.7) [46]

$$\psi_j(\rho) = \left(\frac{\rho}{L_jE_j + H_j\rho}\right)^{1/E_j}, \tag{2.7}$$

where H_j, E_j, and L_j are the coefficients obtained separately per EOS. The interparticle force between node A and its neighbors, as defined in Eq. (2.6), consists of several subforces, as shown in Fig. 1. The number of ψ_j depends on the selected EOS, which is specified in Table 1. By comparing the equation of the state with Eq. (2.7), the constant coefficients of H_j, E_j, and L_j can be obtained as mentioned in Table 1. The pressure in the multi-phase domain can be defined by Eq. (2.8) [46].

$$p = \rho c_s^2 + \sum_{j=1}^{n} \frac{G_jc^2}{2}\left(\frac{\rho}{L_jE_j + H_j\rho}\right)^{2/E_j}. \tag{2.8}$$

Using an analytical method, the density gradient in the x-direction can be calculated using Eq. (2.9) [46]

$$(c\partial_x\rho)^2 = \left(\int_{\rho_v}^{\rho}\left(p_0 - \rho c_s^2 - \sum_{j=1}^{n}\frac{G_jc^2}{2}\psi_j^2\right)\frac{d\rho}{\rho^2}\right) \Bigg/ \left(\frac{a_2}{12\rho^4}\sum_{j=1}^{n} L_j\psi_j^{E_j}\frac{G_jc^2\psi_j^2}{2}\right), \tag{2.9}$$

where a_2 and p_0 are the constant coefficients. By using the force balance (Eq. (2.9)) in the domain, the first component of the pressure tensor (denoted by P_{xx}) can be obtained as

Eq. (2.10b) [46]

$$\sum p\cdot A=\sum F, \tag{2.10a}$$

$$P_{xx}=\sum_{j=1}^{n}\frac{G_jc^2}{2}\psi_j^2+\frac{G_jc^4}{12}\left[\left(a_1+12\Delta ts_jG_j\right)\left(\frac{d\psi_j}{dx}\right)^2+a_2\psi_j\frac{d^2\psi_j}{dx^2}\right], \tag{2.10b}$$

where a_1 and a_2 are constant coefficients and depend on the order of isotropy which is used in the force term. s_j is obtained using the following equation:

$$s_j=-\left(E_ja_2+2a_1\right)/24\Delta tG_j. \tag{2.11}$$

Surface tension can also be calculated by Eq. (2.12)

$$\sigma=\frac{c^4}{12}\sum_{j=1}^{n}\int_{\rho_v}^{\rho_l}G_jM_j\left(\psi_j'\right)^2(\partial_x\rho)d\rho, \tag{2.12}$$

where M_j is assumed by Eq. (2.13)

$$M_j=-3e_4\left(E_j+1\right)-\frac{E_j}{2}-1, \tag{2.13}$$

e_4 is also a constant and considered as follows

$$e_4=\frac{\omega(1)}{2}+2\omega(2)+8\omega(4)+25\omega(5)+32\omega(8)+\cdots. \tag{2.14}$$

For the fourth order isotropy (e_4), only $\omega(1)=1/3$ and $\omega(2)=1/12$ are enough and the rest of the coefficients can be used for the methods with higher orders of isotropy. The fourth order isotropy is employed in the current study; then, e_4 becomes $1/3$ [19, 47]. In multi-pseudo-potential scheme, $Z=(bc^2)/a$ parameter adjusts the interface width without changing the vapor and liquid densities [17]. Reducing Z leads to a reduction in the width of the interface between the two phases. Additionally, Z can be used to increase stability and accuracy of the multi-pseudo-potential scheme.

2.3 Discrete form of intermolecular body forces

The force term discretization method in the lattice Boltzmann model directly affects the accuracy and stability of the solution [12, 48-52]. In 2012, Li et al. [26] examined all the available discrete forms of intermolecular body forces and found that the Guo method [53] was the only method that accurately retrieved the Navier-Stokes equation. Indeed, this method had shallow stability compared with the exact difference method [51]. Accordingly, Li et al. presented a new model that fully recovered the Navier-Stokes equations and had the accuracy and stability of the exact difference method simultaneously

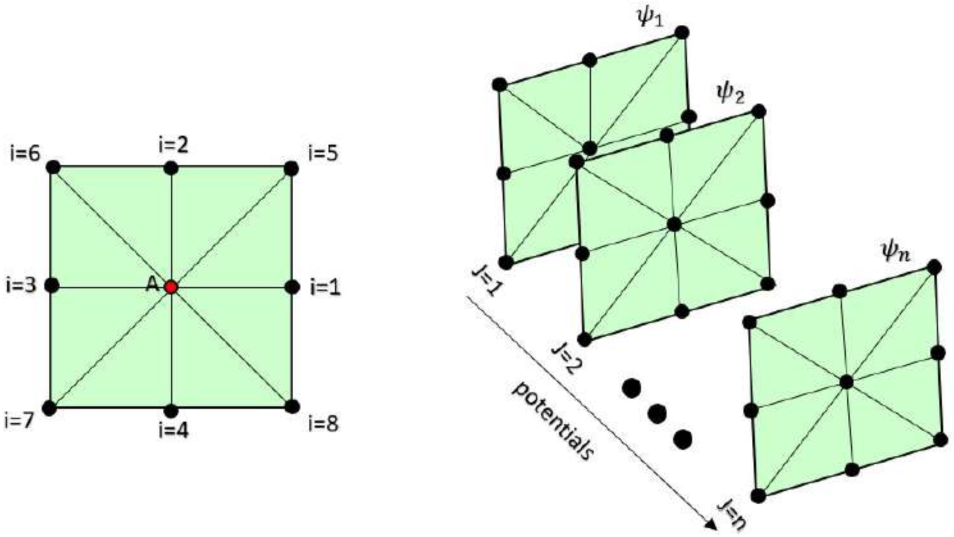

Figure 1: Interparticle pseudo-potentials between node A and its neighbors.

[26]

$$F_i(\mathbf{x},t)=3\omega_i\Delta\left(1-\frac{1}{2\tau}\right)\left[\frac{(e_{i\alpha}-u_\alpha)}{c_s^2}+\frac{3e_{i\alpha}u_\alpha e_{i\beta}}{c_s^4}\right]F_\alpha^{\text{total}}$$
$$+\frac{3\omega_i\Delta t}{2c_s^4}\sum_j^n\left[\frac{s_j}{\tau\psi_j^2}\left(3F_\alpha^{(j)}F_\beta^{(j)}e_{i\alpha}e_{i\beta}-c_s^2F_\alpha^{(j)}F_\alpha^{(j)}\right].\tag{2.15}$$

In this method, the macroscopic and equilibrium velocities used in the force term were as follows:

$$u_\alpha=u_\alpha^{eq}=\sum_i f_ie_{i\alpha}+\frac{F_\alpha\delta t}{2\rho}.\tag{2.16}$$

2.4 EOSs

In this paper, four EOSs of van-der-Waals, Peng-Robinson, Carnahan-Starling, and Soave-Redlich-Kwong are used.

2.4.1 Van der Waals (VdW)

The van der Waals EOS has long attracted researchers' and engineers' attention mainly because of its simplicity and engineering flexibility. In this EOS, a and b are the parameters to explain the force of attraction and repulsion between molecules in real fluids. This equation is considered as follows:

$$p=\frac{\rho RT}{1-b\rho}-a\rho^2\quad\text{or}\quad\left(p+\frac{a}{V^2}\right)(V-b)=RT.\tag{2.17}$$

Table 1: Multi-pseudo-potential scheme parameters for various EOSs.

EOS	ψ_j	G_f	H_j	L_j	E_j
VdW	1	$-2/3$	0	$1/2$	2
	2	$2Tc^{-2}$	$-b$	$1/2$	2
	3	$-2ac^{-2}$	0	1	1
C-S	1	$\left(6Tc^{-2}-2\right)/3$	0	$1/2$	2
	2	$2bTc^{-2}$	$-b/4$	1	1
	3	$b^2Tc^{-2}/4$	$-b/4$	$3/2$	$2/3$
	4	$-2ac^{-2}$	0	1	1
SRK	1	$-\left(2bc^2+6a\alpha\right)/3bc^2$	0	$1/2$	2
	2	$2Tc^{-2}$	$-b$	$1/2$	2
	3	$2a\alpha b^{-1}c^{-2}$	b	$1/2$	2
P-R	1	$-2/3$	0	$1/2$	2
	2	$2Tc^{-2}$	$-b$	$1/2$	2
	3	$\alpha ac^{-2}/b\sqrt{2}$	$b+b\sqrt{2}$	$1/2$	2
	4	$-\alpha ac^{-2}/b\sqrt{2}$	$b-b\sqrt{2}$	$1/2$	2

The critical properties for VdW EOS are $\rho_c=1/3b$, $p_c=a/27b^2$, and $T_c=8a/27Rb$.

2.4.2 Peng–Robinson (P-R)

The Peng–Robinson EOS was proposed in 1976 to provide reasonable accuracy near the critical point as shown below:

$$p=\frac{\rho RT}{1-b\rho}-\frac{a\rho^2\alpha(T)}{1+2b\rho-b^2\rho^2}, \tag{2.18a}$$

$$\alpha(T)=\left[1+\left(0.37464+1.54226\omega-0.26992\omega^2\right)\left(1-\sqrt{T/T_c}\right)\right]^2, \tag{2.18b}$$

where ω is the acentric factor and depends on the kind of fluid; the value of the acentric factor for water is 0.344. The coefficients (a,b) can be calculated by $a=(0.45724R^2T_c^2)/p_c$ and $b=(0.0778RT_c)/p_c$.

2.4.3 Carnahan-Starling (C-S)

In the Carnahan-Starling approach, the molecules are considered as the hard spheres to simulate the intermolecular interaction. The Carnahan-Starling EOS can be stated in the following form:

$$p=\frac{\rho RT\left(1+b\frac{\rho}{4}+\left(b\frac{\rho}{4}\right)^2-\left(b\frac{\rho}{4}\right)^3\right)}{\left(1-b\frac{\rho}{4}\right)^3}-a\rho^2, \tag{2.19}$$

where a and b can be obtained using $a=0.4964R^2(T_c^2)/p_c$ and $b=0.1873RT_c/p_c$.

2.4.4 Soave-Redlich-Kwong (SRK)

Due to its easiness and adequate accuracy, the Soave-Redlich-Kwong EOS is a well-known EOS in modeling and optimizations, in which vapor-liquid equilibrium properties are needed

$$p=\frac{\rho RT}{1-b\rho}-\frac{a\rho^2\alpha(T)}{1+b\rho}, \tag{2.20a}$$

$$\alpha(T)=\Big[1+\big(0.48+1.574\omega-0.176\omega^2\big)\Big(1-\sqrt{T/T_c}\Big)\Big]^2, \tag{2.20b}$$

where a and b can be obtained using $a=0.42748R^2(T_c^2)/p_c$ and $b=0.08664RT_c/p_c$.

2.5 Boundary condition

To consider the zero velocity on the moving wall, a bounce-back type of boundary condition is applied to the non-equilibrium part of the distribution function [54]. Fig. 2 clarifies the boundary condition employed in the current study. The north wall is coinciding with the x-axis and is illustrated by the dotted line in Fig. 2. The unknown values of f_4, f_7, and f_8 pointing outwards with respect to the wall are to be obtained by employing the after-streaming values of f_0, f_1, f_2, f_3, f_5, and f_6. Assuming that u_N and v_N are specified on the northern wall, Eqs. (2.21a)-(2.21c) are used to calculate f_4, f_7, f_8, and ρ_N

$$\rho_N=f_0+f_1+f_2+f_3+f_4+f_5+f_6+f_7+f_8, \tag{2.21a}$$

$$\rho_N u_N=f_1+f_5+f_8-f_6-f_3-f_7, \tag{2.21b}$$

$$\rho_N v_N=f_5+f_2+f_6-f_7-f_4-f_8, \tag{2.21c}$$

where subscript N indicates the northern wall, as shown in Fig. 2. From the bounce-back idea used to the non-equilibrium part of the particle distribution normal to the wall, it is known that $f_2-f_2^{eq}=f_4-f_4^{eq}$. This can change the set of Eqs. (2.21a)-(2.21c) to a closed form, as detailed in Eqs. (2.22a)-(2.22d)

$$f_4=f_2-\frac{2}{3}\rho_N v_N, \tag{2.22a}$$

$$\rho_N=\frac{1}{1+v_N}\left[f_0+f_1+f_3+2(f_2+f_6+f_5)\right], \tag{2.22b}$$

$$f_7=f_5+\frac{1}{2}(f_1-f_3)-\frac{1}{6}\rho_N v_N-\frac{1}{2}\rho_N u_N, \tag{2.22c}$$

$$f_8=f_6+\frac{1}{2}(f_3-f_1)+\frac{1}{2}\rho_N u_N-\frac{1}{6}\rho_N v_N. \tag{2.22d}$$

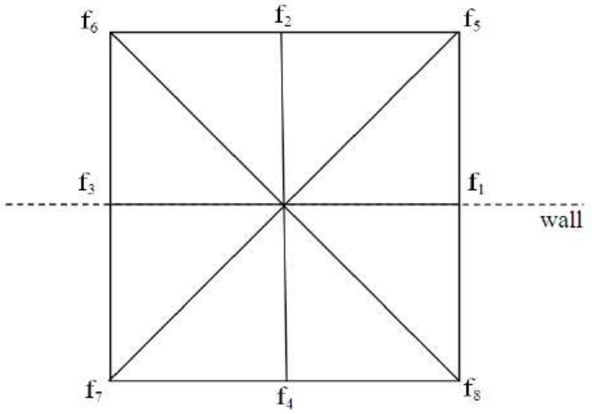

Figure 2: Distribution function for D2Q9 configuration on the northern moving wall.

3 Bubble and droplet deformation in shear flow

Shear flows are divided into three types: simple shear flow [27, 32-35, 38, 40, 41, 55], plane hyperbolic (stagnation point) flow [30, 56, 57], and orthogonal-rheometer flow [58-60]. The shear flow in the present study is of simple shear flow type. Bubbles and droplets deform when subjected to shear stress, which is affected by the surface tension (σ), suspending or continuous phase viscosity (μ), suspended or dispersed bubble or droplet viscosity (μ'), shear rate $(\dot{\gamma})$, and radius of the bubble or droplet before deformation (r). Based on Buckingham Pi theorem, the following dimensionless numbers can be used to analyze the bubble deformation [61]:

$$Ca=\frac{\mu\dot{\gamma}r}{\sigma}, \tag{3.1a}$$

$$\lambda=\frac{\mu'}{\mu}, \tag{3.1b}$$

where Ca and λ are the capillary number and viscosity ratio, respectively. The shear rate for the flow between the two parallel moving plates separated by distance H can be calculated as follows:

$$\dot{\gamma}=U/H, \tag{3.2}$$

where U is the velocity of plates. Taylor [27] introduced parameter D to determine the amount of bubble and droplet deformation as follows:

$$D=\frac{L-B}{L+B}. \tag{3.3}$$

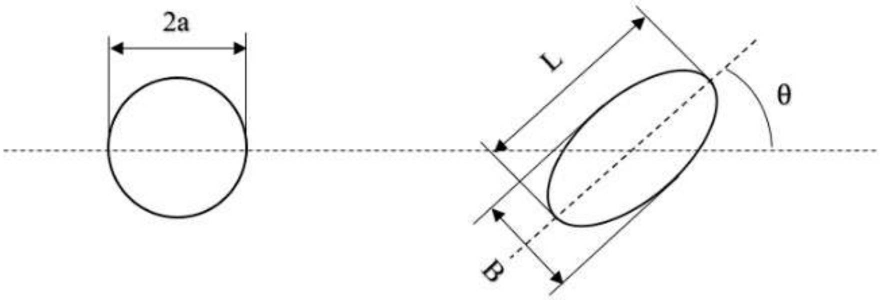

Figure 3: Characteristics of deformed bubble (droplet) geometry at Ca$<$1.

Parameters L and B are specified in Fig. 3. The value of parameter D varies from zero to one. For a spherical bubble droplet (without deformation), the value of D is zero. For a large deformation bubble, this value will be close to one.

3.1 Small deformation (Ca <1)

The stable shape of the bubble or droplet in the small deformation range can be described using Taylor's theory, the relation of which is as follows [27]:

$$D=Ca\frac{19\lambda+16}{16\lambda+16}. \tag{3.4}$$

According to Taylor's article, Eq. (3.4) can be used for all values of the viscosity ratio (λ)- from zero to infinity and the capillary range of $Ca<1$ [36, 57]. Later, Canedo et al. [38] and Rust and Manga [40] have shown that Eq. (3.4) is only valid for $Ca<0.5$ and has a significant error outside of it [38].

The orientation of the bubble or droplet to the main flow is defined by angle θ between the principal axis of the bubble (longest dimension) and the wall direction (Fig. 3). Rallison [34] presented Eq. (3.5) at $Ca<1$ and $\lambda<1$ for parameter θ as follows:

$$\theta=\pi/4-0.6Ca. \tag{3.5}$$

Cox conducted an extensive study on the simultaneous capillary number and viscosity ratio on droplet deformation [29]. He assumed that the viscosity ratio was greater than one and proposed the following equations for D and θ:

$$D=\frac{5(19\lambda+16)}{4(\lambda+1)\sqrt{(20k)^2+(19\lambda)^2}}, \tag{3.6a}$$

$$\theta=\frac{\pi}{4}-\frac{1}{2}\arctan\left(\frac{19\lambda Ca}{20}\right), \tag{3.6b}$$

where k is the inverse of the capillary number.

3.2 Large deformation $(Ca>1)$

The large deformation of the bubble or droplet is entirely dependent on the amount of viscosity ratio. Torza et al. concluded that the droplet would never undergo a large deformation assuming $\lambda>1$ [31]. Several investigations have been performed about the deformation of the bubble in the condition of $\lambda<0.2$ [33, 38, 40, 41]. In this situation, the bubble stretches to a large extent, and observations show that the final length of the bubble reaches about ten times of the initial radius [31, 33, 38, 40, 41]. In this case, the bubble's shape resembles slender, so that the end of the bubble looks like a sharp point. In the intermediate range $(0.2<\lambda<1)$, studies have shown that the length of the bubble eventually reaches four times of the initial radius [31]. In this case, the tip of the bubble takes on a circular shape. It must also be noted that, in all the cases, from a particular time onwards, the shape of the bubble no longer changes and reaches a steady state. Hinch and Acrivos [33] introduced the geometric parameters of the final deformed bubble for the large deformation model in Fig. 4. They presented the following relations for the geometric characteristics of the deformed bubble:

$$\frac{L}{a}=3.45\text{Ca}^{1/2}, \tag{3.7a}$$

$$\theta=\arctan\left(0.359\text{Ca}^{-3/4}\right). \tag{3.7b}$$

Canedo et al. [38] corrected the dimensionless length relation provided by Hinch and Acrivos (Eq. (3.7a)) as follows:

$$\frac{L}{a}=3.1Ca^{0.43}. \tag{3.8}$$

It must be noted that Eq. (3.6a) and Eq. (3.6b) are not limited to small deformations and can be used to calculate parameters D and θ in the large deformation range of a droplet.

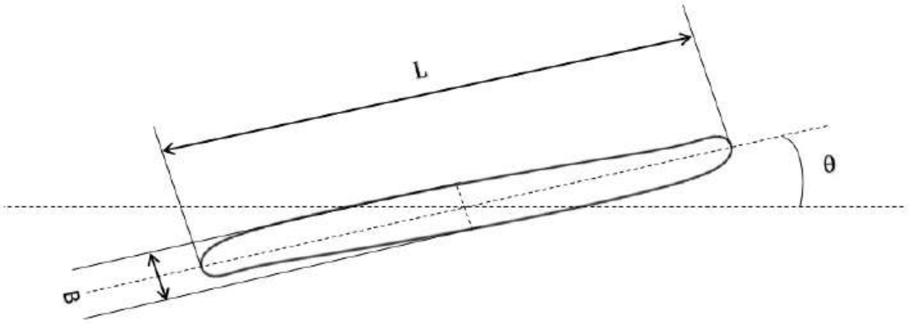

Figure 4: Characteristics of deformed bubble (droplet) geometry at $Ca>1$ [33].

3.3 Breakup

When the capillary number exceeds the critical capillary number, the bubble (droplet) becomes very thin and, eventually, breaks into a few smaller bubbles (droplets) [34]. The shape of the remaining bubbles will be fixed after a certain period of time [34]. Torza et al. [31] concluded that during the interval $0.2 \leq \lambda \leq 3$, as the viscosity ratio increased, the critical capillary number decreased and the bubble (droplet) broke up faster. However, in the range of $\lambda < 0.2$, the bubble became more resistant to breakup and the critical capillary number decreased with increasing viscosity ratio. Their results also showed that the bubble did not break up at the viscosity ratio greater than 3. They observed that the critical capillary number within $0.2 \leq \lambda \leq 2.2$ was much smaller than the critical capillary number in the range of $\lambda < 0.2$.

4 Results

In this section, a flat interface and static droplet problems are studied by using the multi-pseudo-potential Shan-Chen model. The relaxation time for these studies is set to one. The fourth order isotropy is also used to calculate the discretized force term. The constants of the EOS are considered as $a = 0.02$ and $b = 0.3$. Boundaries are assumed to be periodic. The quantities of length and time are in lattice units. The size of lattice for both kinds of problems is 200×200. Afterwards, the droplet and bubble deformation under simple shear flow are studied. The VdW EOS is used for these simulations. The constant coefficients of VdW EOS are assumed to be $a = 9/49$ and $b = 2/21$. Calculations are performed for three capillary number ranges: low (small deformation), medium (large deformation), and high (breakup) for both droplets and bubbles.

4.1 Flat interface and static droplet problem

In the case of the flat interface, according to the mechanical stability, the total normal component of the pressure tensor $(P_0 = P_{xx} + \rho\theta)$ must remain constant in the direction perpendicular to the interface [62]. As mentioned before, the x component of the pressure tensor (P_{xx}) can be obtained from Eq. (2.10b). The results of the total normal component of the pressure tensor are shown in Fig. 5 for various EOSs. As can be seen, the mechanical stability criterion is satisfied and the normal component of the pressure tensor is constant across the phase interface. The density distribution in the direction perpendicular to the interface can also be calculated analytically using Eq. (2.9). In Fig. 6, the numerical simulation of density distributions across the phase interface is compared with the values obtained from the analytical solution for the equation of VdW, P-R, and SRK. As can be seen, the numerical results are in good agreement with the analytical ones at different reduced temperatures.

Physical observations show that the thickness of the interface layer between the two phases is much smaller than the spatial step dimension in the typical numerical sim-

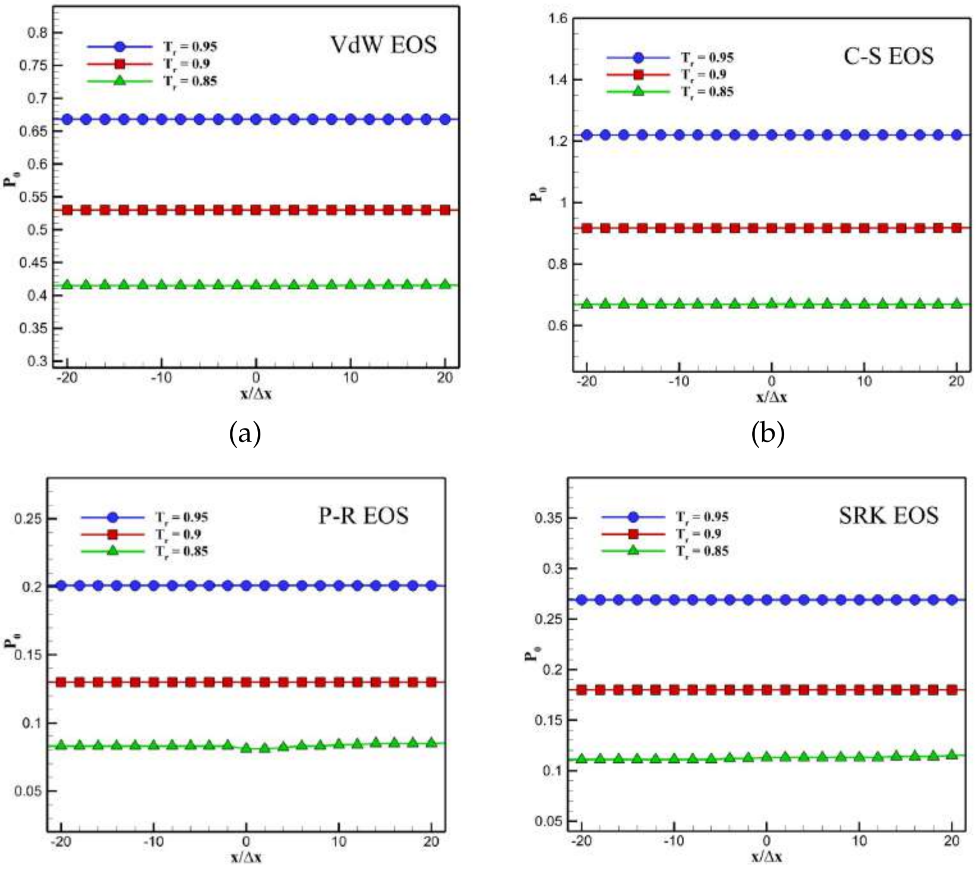

(a) (b)

(c) (d)

Figure 5: Total normal component of the pressure tensor across the phase interface for the EOS of C-S (a), VdW (b), P-R (c), and SRK (d).

ulations. Such a small value cannot be captured by the methods which are based on the diffuse interface theory (e.g., LBM). According to Fig. 7, in the present simulation, the thickness of the interface layer can be detected from the density distribution results across the interface. As mentioned earlier, in the current model, the thickness of the interface layer at the constant reduced temperature (Tr) depends only on the parameter of $Z=(bc^2)/a$. In the following, the effect of parameter Z on the thickness of the interface layer is investigated. Fig. 7 shows a comparison of the numerical and theoretical results (Eq. (2.9)) of the density distribution in the direction perpendicular to the interface at the reduced temperature of 0.75 employing EOS of VdW and P-R. This figure demonstrates that the numerical and theoretical values are in good agreement with each other. As mentioned before, based on (Eq. (2.9)), the present model can adjust the thickness of the interface layer independent of the reduced temperature. In Fig. 7, it is shown that

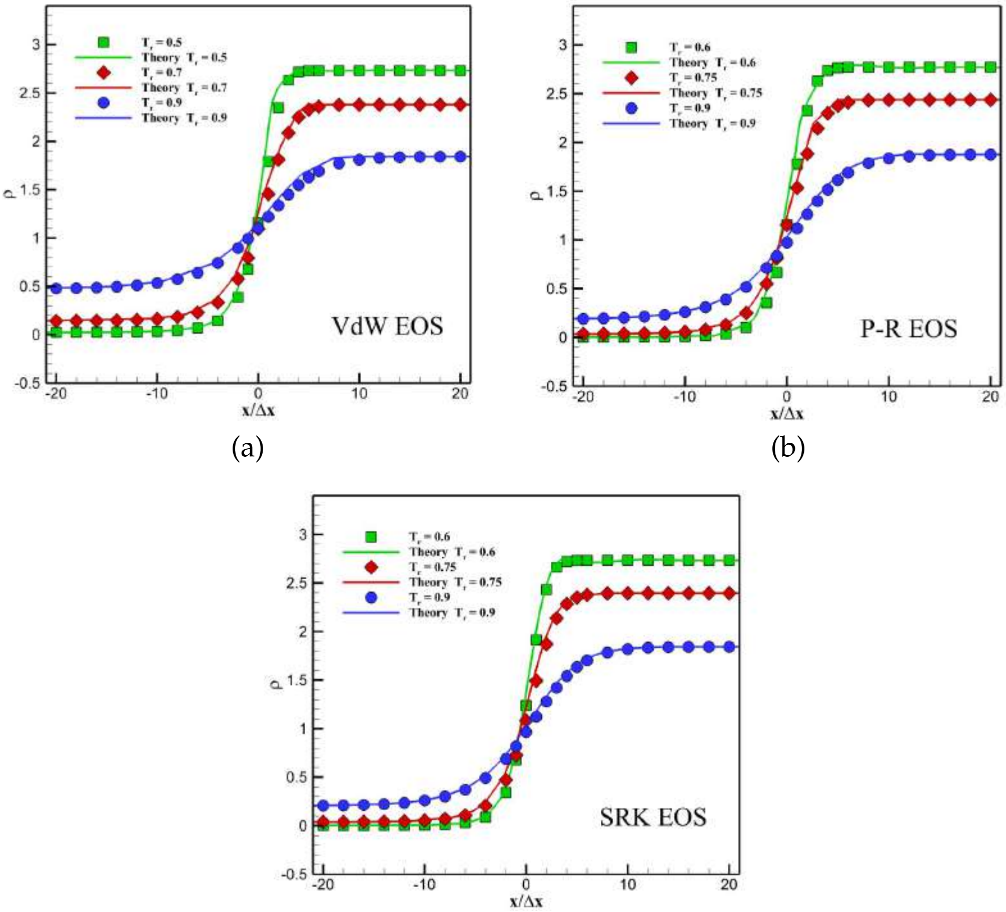

(a) (b)

(c)

Figure 6: Numerical and theoretical simulations of density distributions across the phase interface at different various reduced temperatures for the EOS of VdW (a), P-R (b), and SRK (c).

increasing the value of Z leads to an increment in the interface layer thickness. Current simulations show that the thickness of the interface layer is effective in the accuracy and stability of the solution. In other words, increasing Z can cause an increase in stability and computational accuracy.

The coexistence densities of the vapor-liquid equilibrium are obtained for static droplets using the multi-pseudo-potential Shan-Chen scheme in Fig. 8. Numerical values are compared with the values obtained from Maxwell's solution (which is an accurate solution for calculating coexistence densities in two-phase flows [3]). The results indicate the present model has thermodynamic consistency up to the density ratio of about 1.26×10^6 using the EOS of VdW. The effect of interface layer thickness ($\Gamma = |x_{(\rho=0.98\rho_l)} - x_{(\rho=1.02\rho_v)}|$) on the amount of two-phase densities is also investigated.

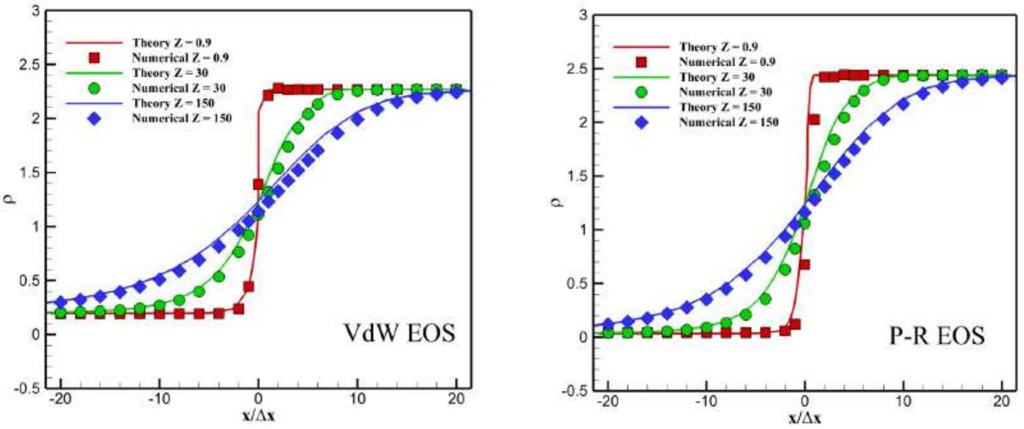

(a) (b)

Figure 7: Numerical and theoretical simulations of density distributions across the phase interface at $Tr=0.75$ for the EOS of VdW (a) and P-R (b).

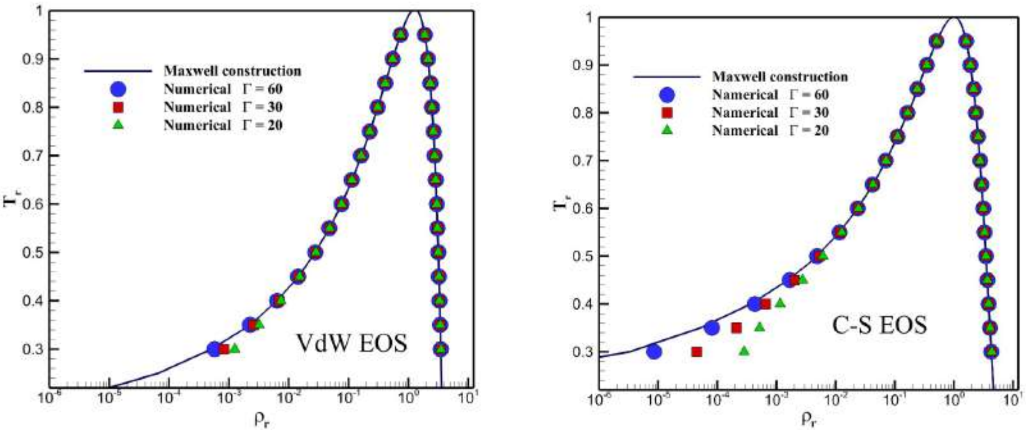

(a) (b)

Figure 8: Comparing the coexistence of the vapor-liquid equilibrium densities between the numerical and Maxwell's solution for the equation of VdW (a) and C-S (b).

Accordingly, the thickness of the interface layer has a significant effect on the accuracy of the present model with the EOS of C-S at low reduced temperatures. In this case, by considering $\Gamma=60$, it is possible to achieve acceptable accuracy at the density ratio of 10^6.

Next, the Laplace test is performed at a constant reduced temperature $(Tr=0.8)$. This test is executed to calculate the surface tension values from the numerical results of the stationary droplet [63]. In this test, the pressure difference between the inside and outside of the droplet is plotted with the inverse droplet radius. The slope of the drawn line is

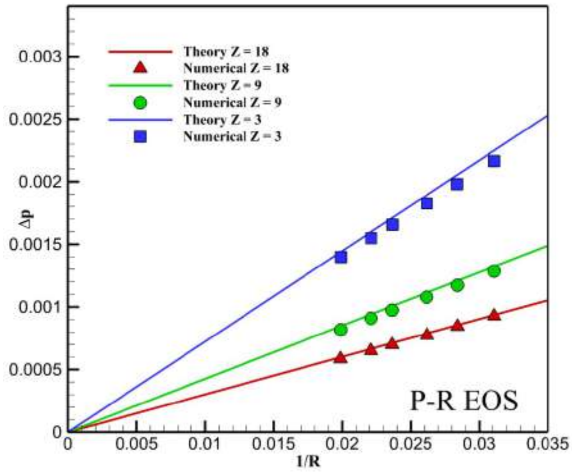

Figure 9: Comparing surface tension calculated by Laplace test (numerical) and theoretical solution using the EOS of P-R for $Tr=0.8$.

equal to the surface tension. Comparison of surface tension calculated by the Laplace test and theoretical solution (Eq. (2.12)) by employing the EOS of P-R is illustrated in Fig. 9. The results demonstrate that the present model converges to surface tensions from 0.03 to 0.0723 under the mentioned conditions.

The value of the spurious velocity for different EOSs in terms of the reduced temperature is displayed in Fig. 10. As can be seen, the amount of spurious velocity increases with decreasing the reduced temperature. In this figure, the effect of the interface layer thickness (Γ) on the amount of spurious velocity is also investigated. The results illustrate that with increasing the thickness of the interface layer, the amount of spurious velocity decreases. By taking into account the equation of VdW and reduced temperature of 0.35, the value of the spurious velocity is close to 10^{-3}. This shows the present model could significantly reduce the amount of spurious velocity compared with single-pseudo-potential Shan-Chen schemes at low reduced temperatures.

4.2 Droplet and bubble deformation under simple shear flow

In this section, bubble ($\lambda<1$) and droplet ($\lambda>1$) deformation is simulated under a simple shear flow. Eq. (3.3) is used to calculate parameter D for the droplet (bubble). In Fig. 11, the variation of the critical capillary number versus the viscosity ratio is investigated for $0.5<\lambda<2.5$. Accordingly, as the viscosity ratio increases, the critical capillary values decrease. In terms of small and large deformation, the numerical results are compared with the experimental and analytical equations presented in Sections 4.2.1 and 4.2.2.

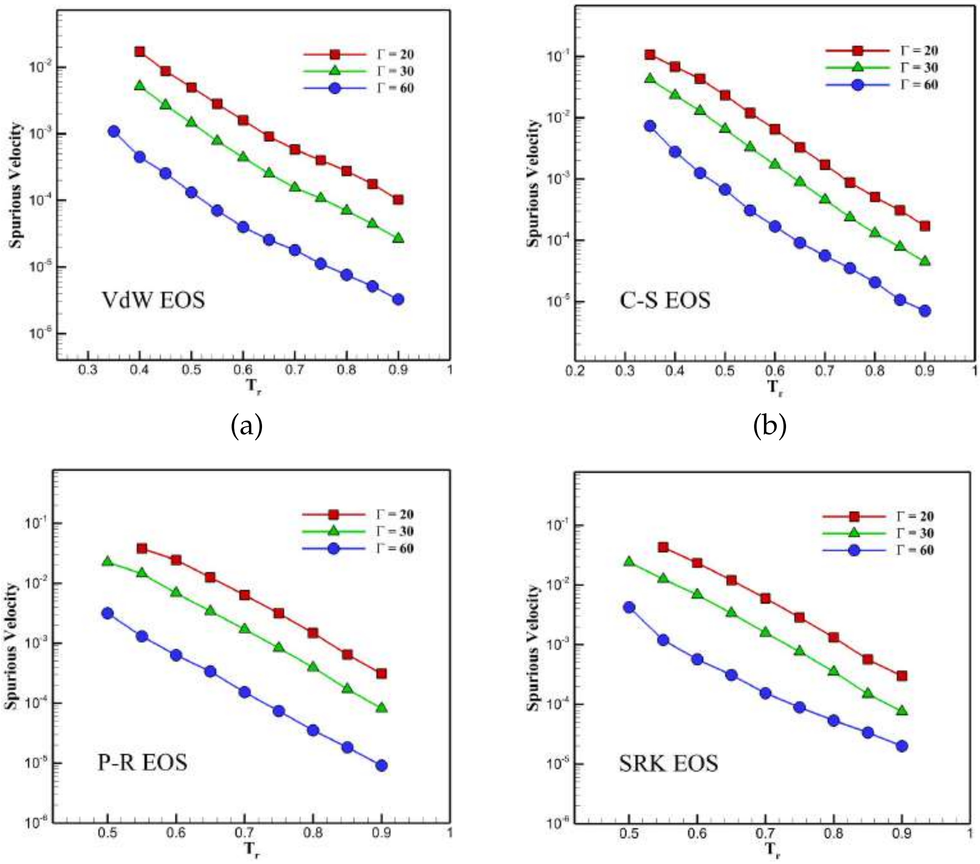

(a) (b)

(c) (d)

Figure 10: Spurious velocity in the phase interface employing equation of VdW (a), C-S (b), P-R (c), SRK (d).

4.2.1 Droplet deformation

The simulations show that the droplet shape under the simple shear flow never reaches the slender body, which has been confirmed by previous experimental studies [29, 31]. Therefore, three configurations for droplet deformation are drawn in Fig. 12. Fig. 12(a) shows the small deformation of the droplets in different sequences for $\lambda=5$ and $Ca=0.19$. The results illustrate that the droplet reaches an elliptical shape after 5000 steps and, then, this shape remains constant. The large deformation of a droplet is depicted for $\lambda=1.9$ and $Ca=4.6$ in Fig. 12(b). Under these conditions, the opposite effect of shear and surface tension forces is well observed. The figure displays that the droplet reaches its maximum elongation in the step of about 8000. In this state, the surface tension force tends to return the droplet to its original shape. Therefore, after about 14000 steps, the shape of the droplet changes to an elliptical formation. This state is also unstable and

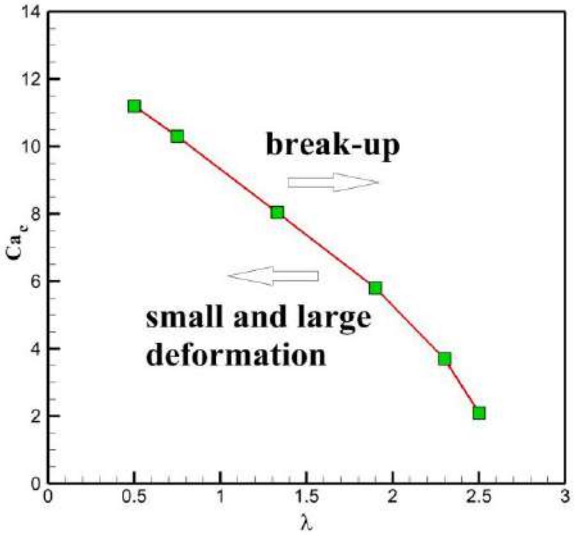

Figure 11: Critical capillary numbers versus viscosity ratio.

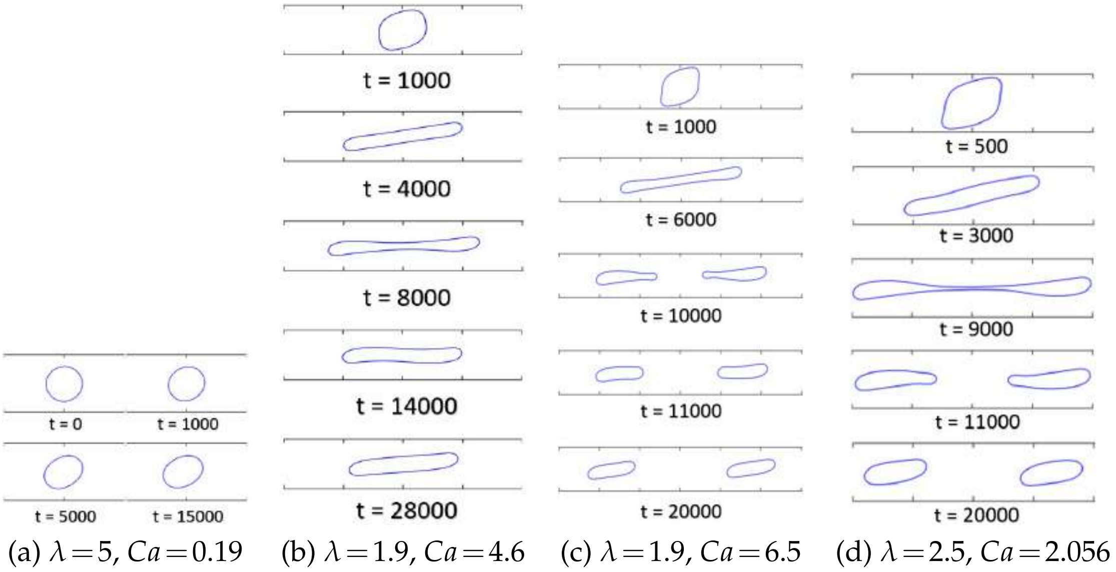

(a) $\lambda = 5$, $Ca = 0.19$ (b) $\lambda = 1.9$, $Ca = 4.6$ (c) $\lambda = 1.9$, $Ca = 6.5$ (d) $\lambda = 2.5$, $Ca = 2.056$

Figure 12: Droplet deformation in different conditions: (a) small deformation, (b) large deformation, (c), (d) breakup.

the shear forces cause the droplet to stretch again. Finally, in the time step of 28000, the last shape of the droplet is obtained. This type of oscillation is seen frequently in the large deformations of the droplet. The length of the final shape is about four times of the original radius. As mentioned, this length indicates the droplet shape has not entered

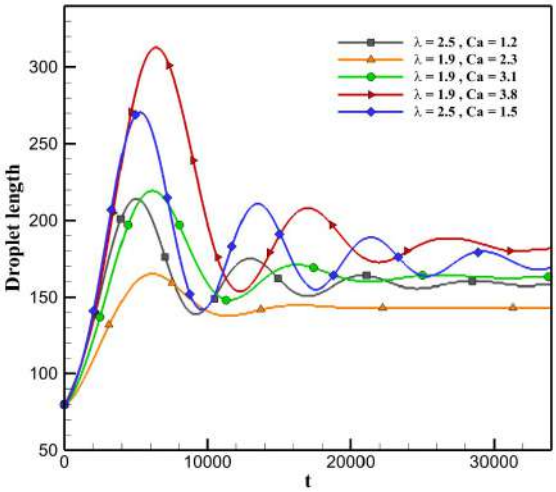

Figure 13: Droplet oscillation versus time in different capillary numbers and viscosity ratios.

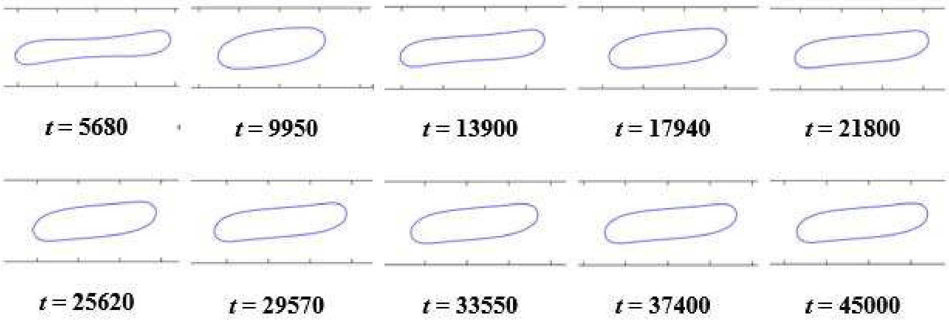

Figure 14: Droplet oscillation at $\lambda = 2.5$ and $Ca = 1.5$.

the slender state. Figs. 12(c) and (d) illustrate the breakup process of the droplet for $\lambda = 1.9$, $Ca = 6.5$ and $\lambda = 2.5$, $Ca = 2.056$. As can be seen, in both cases, the surface tension force is not strong enough to hold the droplet as a single droplet and breakup occurs in the time step of 10000 for $\lambda = 1.9$ and $Ca = 6.5$, and time step of 9500 for $\lambda = 2.5$ and $Ca = 2.056$. The results show that the deformation rate is more dependent on the viscosity ratio than on the capillary number. As the viscosity ratio increases, the deformation rate increases as well. On the other hand, the capillary number affects the final deformation. As expected, increasing the capillary number reduces the elongation of the final shape of the droplet. The present model results show that in all capillary numbers larger than the critical capillary number, the droplet is eventually broken up into two parts.

Fig. 13 shows the change in droplet length (L) over time until constant length is reached at different capillary numbers and viscosity ratios. The droplet is continuously

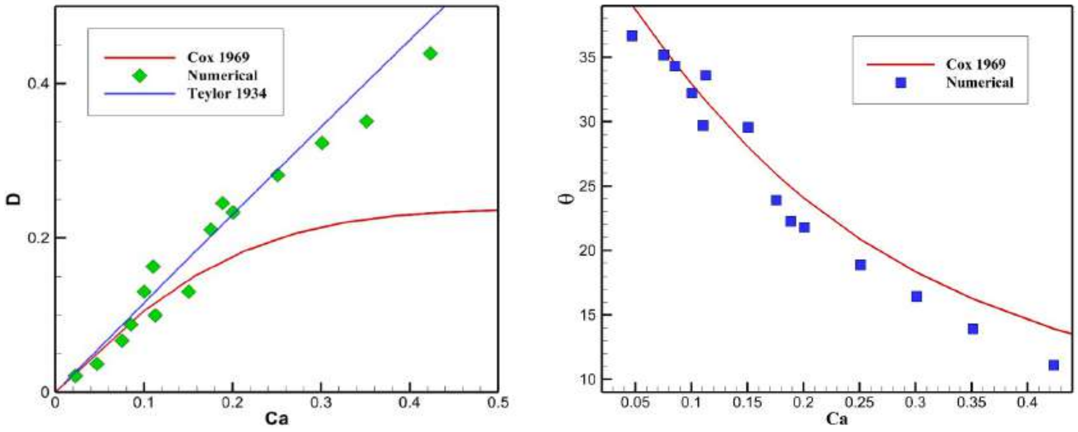

(a) (b)

Figure 15: Comparison between numerical and experimental results (Cox 1969 [29] and Taylor 1934 [27]) for parameters of D (a) and θ (b) at $\lambda = 5$.

stretched and contracted at all capillary numbers and viscosity ratios to get its constant size. According to this figure, at the capillary number of 3.8 and viscosity ratio of 1.9, the droplet length initially reaches the length equal to four times of the initial radius. Eventually, it converges to the length equal to 2.28 of the initial radius. As the capillary number decreases, the amplitude of the length fluctuations also diminishes and, eventually, the final length of the droplet is reduced. Decreasing the capillary number also reduces the number of droplet length oscillations. It can lead to less time for the droplet to reach the constant length. Fig. 14 shows a schematic of the droplets at peak and low times for the capillary number of 1.5 and viscosity ratio of 2.5. As can be seen, after the time of about 37400, the droplet length changes are negligible and it can be assumed that the droplet reaches the constant length.

In the following, we will examine the effect of capillary number on the final shape of the droplet. Fig. 15 shows the numerical and experimental results of D and θ for low capillary numbers. In Fig. 15(a), numerical results of D are compared with the experimental values obtained from the Taylor relation [27] and Cox equation [29] at $Ca < 0.5$ and $\lambda = 5$. As can be seen, the numerical results for parameter D are in acceptable agreement with the Taylor relation (Eq. (3.4)). However, the numerical values of D parameter deviate significantly from the Cox equation (Eq. (3.6a)). It shows that the Cox relation is not suitable for estimating parameter D in the capillary number less than 0.5. Fig. 15(b) indicates the variation of θ versus the capillary number. The numerical and experimental methods estimate the depicted values of θ. Results show that the numerical results of θ are in reasonable agreement with the Cox values, which are calculated by Eq. (3.6b).

Fig. 16 shows the effects of capillary number and viscosity ratio on the value of parameters of D and θ in the middle range of capillary number. According to Fig. 11, the

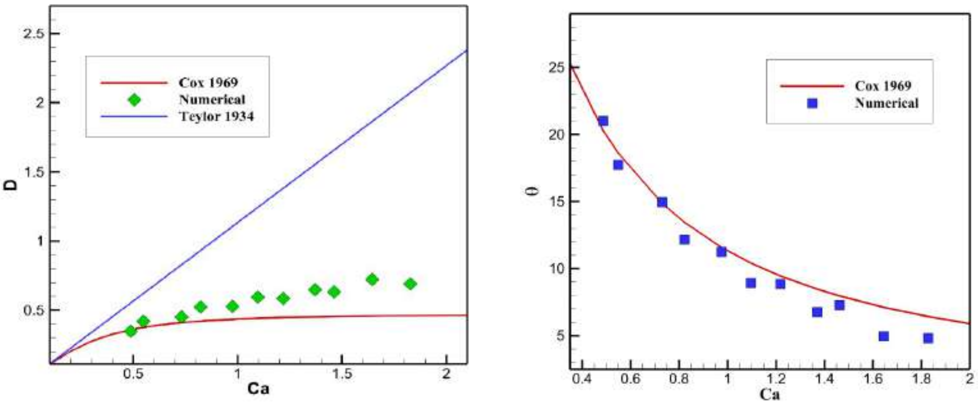

(a) $\lambda = 2.5$ (b) $\lambda = 2.5$

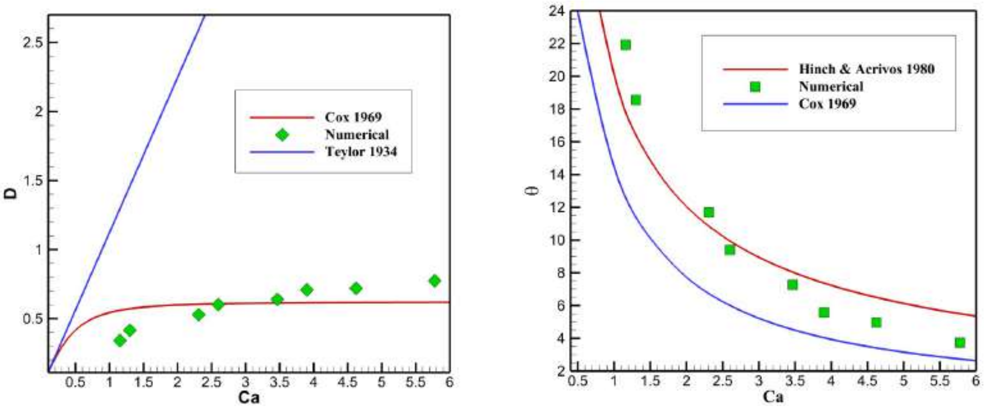

(c) $\lambda = 1.9$ (d) $\lambda = 1.9$

Figure 16: Comparison between numerical and experimental results (Cox 1969 [29] and Taylor 1934 [27]) for parameters of D (a), (c) and θ (b), (d) at $\lambda = 2.5$ (a), (b) and $\lambda = 1.9$ (c), (d).

critical capillary number for $\lambda = 2.5$ and $\lambda = 1.9$ is close to 2.1 and 5.9, respectively. Therefore, Figs. 16(a) and (b) are drawn in the interval of $0.5 < Ca < 1.85$ and Figs. 16(c) and (d) are illustrated in the interval of $1 < Ca < 5.9$. As can be seen, the numerical values of D and θ are consistent with the results of the Cox relation [29]. However, as the amount of capillary numbers increases, the distance between D's numerical and experimental values increases. At $\lambda = 1.9$, the numerical results of D are still in good agreement with the Cox relation values. However, the calculated values of θ at $\lambda < 2$ are close to the experimental results by Hinch and Acrivos [33]. At $\lambda > 2$, the results of θ are placed between the Cox and Hinch and Acrivos estimations, so that as λ increases, the numerical values of θ tend to the Cox relation.

4.2.2 Bubble deformation

In this section, the deformation of the bubble with the viscosity ratio in the interval of $0.2 < \lambda < 0.6$ is examined. Taylor equation (Eq. (3.4)), Hinch and Acrivos equation (Eq. (3.7a)), and Canedo equation (Eq. (3.8)) are used to evaluate the geometric parameters related to the bubble deformation. As mentioned, Taylor relation is helpful for small deformations, while Hinch and Acrivos and Canedo equations are applied for large de-

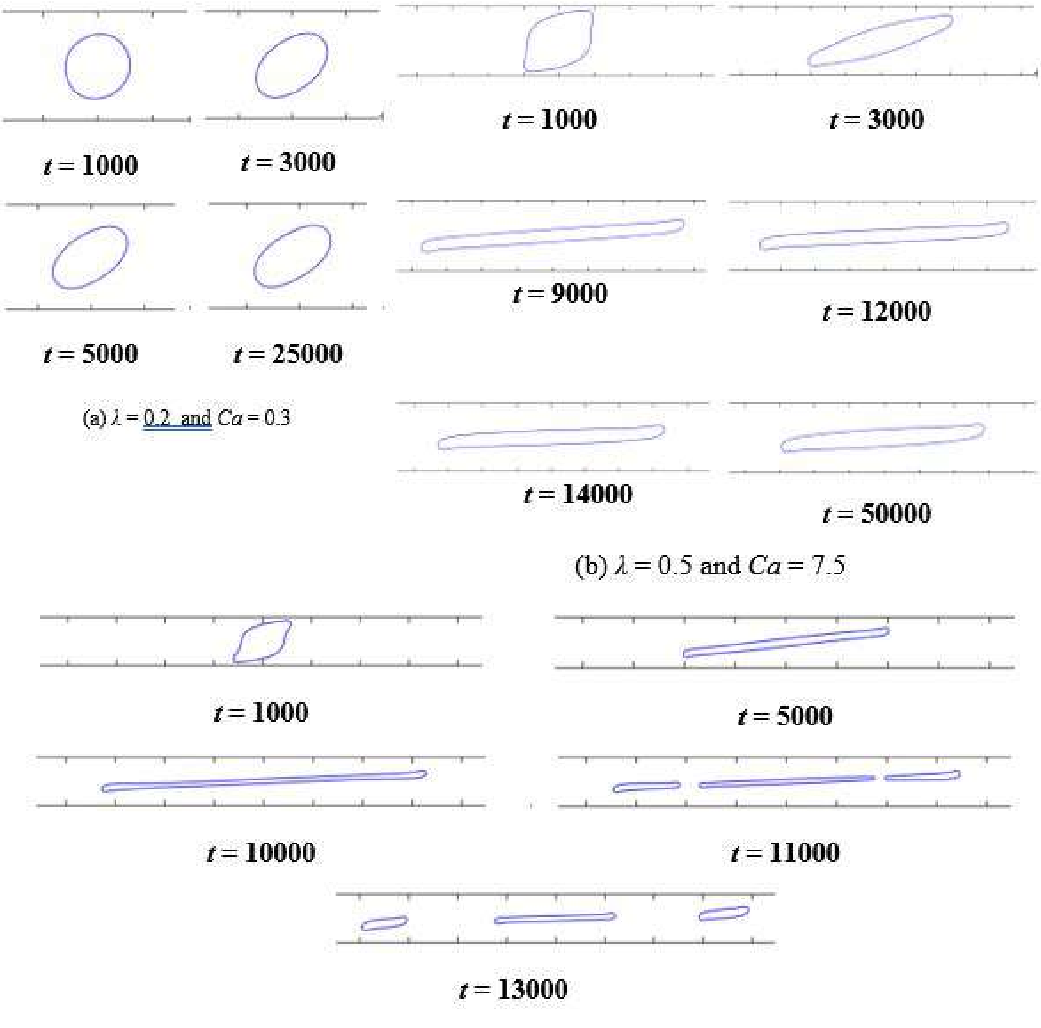

(a) $\lambda = 0.2$ and $Ca = 0.3$

(b) $\lambda = 0.5$ and $Ca = 7.5$

(c) $\lambda = 0.5$ and $Ca = 11.2$

Figure 17: Bubble deformation in different conditions: (a) small deformation, (b) large deformation, and (c) breakup.

formations. Fig. 17 shows the bubble deformation in three categories small deformation, large deformation, and breakup, respectively. As shown in Fig. 17(a), the final shape of the bubble at $\lambda=0.2$ and $Ca=0.3$ is elliptical. The results show that the bubble shape gradually turns into an elliptical formation in the small deformation interval. However, during the large deformation, it oscillates between the initial and final formations. An example of this oscillation for a bubble with λ=0.5 and Ca=7.5 is illustrated in Fig. 17(b). In this model, the length of the bubble is stretched until the time step of 9000 reaches about five times of the initial radius. Afterwards, the length of the bubble decreases and, then, increases until reaching the equilibrium at the length equal to about four times of the initial radius. Compared with the droplet results, it can be concluded that a higher capillary number is needed for the bubble to achieve the same final formation as the droplet. According to Fig. 11, the value of the critical capillary number for λ=0.5 is about 11.2. Thus, the bubble breakup is simulated for $Ca=11.2$, which is shown in Fig. 17(c). As shown in the figure, the bubble eventually breaks up into three parts.

For the bubbles, the deformation parameters of D and θ in different capillary numbers are shown in Fig. 18. For the lower capillary numbers, the numerical results are in good agreement with the Taylor relation (Eq. (3.4)). For capillary numbers greater than 0.5 to about 4, the relation of Hinch and Acrivos (Eq. (3.7a)) is suitable. In capillary numbers larger than 4, the results are entirely consistent with the Canedo equation (Eq. (3.8)). The value of angle θ is plotted versus the capillary number for the bubble in an equilibrium state. As can be seen, the results obtained in values of capillary numbers lower than one are in good agreement with the Rallison relationship (Eq. (3.5)) and, in values of capil-

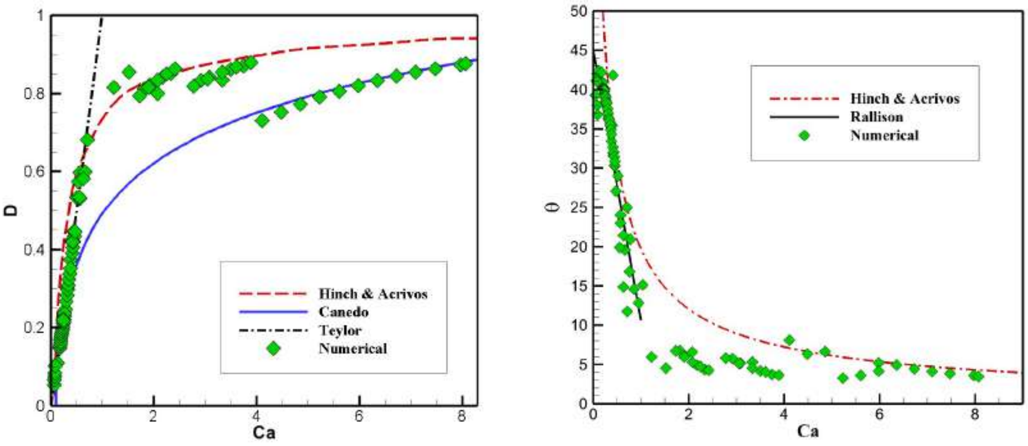

(a) (b)

Figure 18: Comparison between numerical and experimental results for the parameters of D (a) and θ (b) versus capillary numbers.

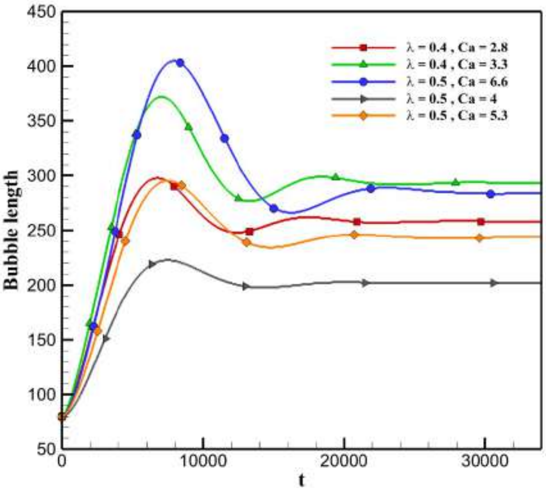

Figure 19: Bubble oscillation at different capillary numbers and viscosity ratios.

lary numbers higher than one, they are consistent with the Hinch and Acrivos relation (Eq. (3.7b)).

Fig. 19 shows the change in the length of bubbles (L) over time until reaching constant length at different capillary numbers and viscosity ratios. For a bubble at the capillary number of 6.6 and viscosity ratio of 0.5, the length initially reaches five times of the initial radius. Eventually, it converges to about 3.56 times of the initial radius. As the capillary number decreases, the amplitude of the length fluctuations also decreases, leading to a reduction in the final length of the bubble. The number of bubble oscillations until reaching the final length is less than the droplet. Fig. 20 shows a schematic of the bubble at peak and bottom times for the capillary number of 3.3 and viscosity ratio of 0.4. As expected, the bubble deformation is greater than the droplet deformation under similar conditions.

5 Conclusions

In the present study, we first evaluated the combination of a multi-pseudo-potential LBM with the discrete form of intermolecular body force of Li et al. in the flat interface and static droplet problems. It was shown this model had excellent thermodynamic consistency using the EOS of van der Waals. Current results demonstrated that the thickness of the interface layer had a significant effect on the accuracy and stability of the multi-pseudo-potential model. Moreover, the present model could adjust the thickness of the interface layer and surface tension independent of the reduced temperature and EOS. Therefore, the present model had the potential to simulate different problems under different conditions with acceptable accuracy.

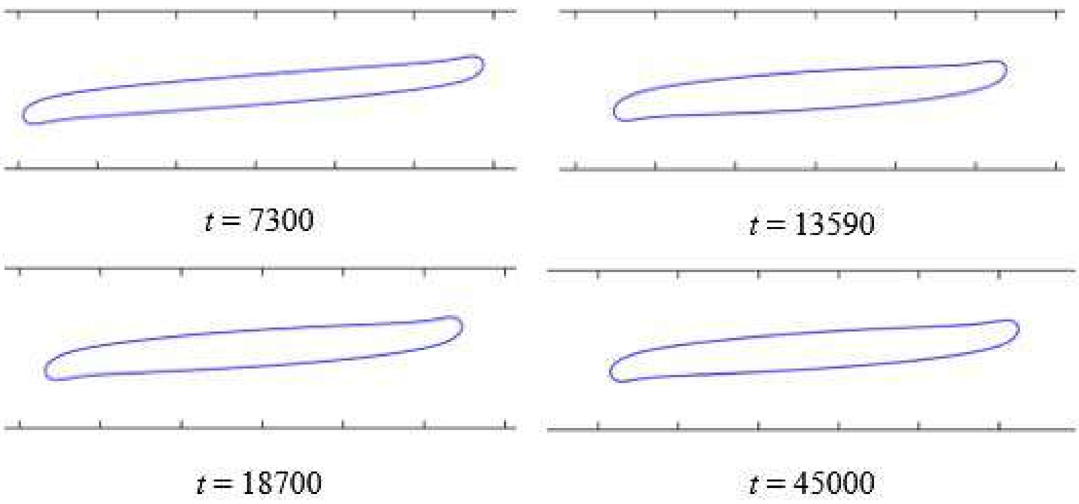

Figure 20: Bubble oscillations at $\lambda = 0.4$ and $Ca = 3.3$.

Secondly, the droplet and bubble deformation and breakup were investigated by the presented multi-phase LBM. When a bubble or droplet was subjected to a shear flow, it underwent an oscillating deformation. The droplet and bubble underwent a series of elongations and contractions to reach their final length. Various scenarios, including small deformation, large deformation, and breakup for bubbles $(0.2<\lambda<1)$ and droplets $(1<\lambda<5)$ were separately studied. In this study, the viscosity ratios of $0.2<\lambda<8$ and capillary numbers of $0<Ca<12$ were investigated. The deformation characteristics were accurately evaluated and more appropriate theoretical and experimental relationships were introduced for different ranges of capillary numbers and viscosity ratios.

The droplet and bubble would be elliptical in the small deformation interval $(Ca<1)$, as confirmed by all the experimental references. The current numerical results were in good agreement with the results of Taylor's theory. In the droplet problem, when the capillary was less than 0.5, the value of D was consistent with the Taylor equation (Eq. (3.4)); when the capillary was greater than 0.5, it was consistent with the Cox relation (Eq. (3.6a)). For parameter θ, the results of the present model corresponded to the Cox equation (Eq. (3.6b)) and Hinch and Acrivos equation (Eq. (3.7b)) for $\lambda>2$ during all the capillary numbers and $\lambda<2$ within $Ca>1$, respectively. For the bubble deformation, parameter D with respect to $Ca<1$, $1<Ca<4$, and $Ca>4$ corresponded to the Taylor relation (Eq. (3.4)), the Hinch and Acrivos relation (Eq. (3.7a)), and the Canedo relation (Eq. (3.8)), respectively. For angle θ, the numerical results were consistent with the Rallison relation (Eq. (3.5)) and the relation of Hinch and Acrivos (Eq. (3.7b)) considering $Ca<1$ and $Ca>1$, respectively. In a large deformation scenario, if the viscosity ratio was less than 0.2, the bubble stretched and its tip sharpened. When the viscosity ratio was greater than 0.2, unlike the previous case, the tip of the bubble and droplet took on a circular shape. The results showed that the number of oscillations of the bubble until reaching the final length was less than the droplet and the bubble reached the final shape in less time than the droplet.

Nomenclature

Coefficients of pressure tensor equation	a_1, a_2
Constant parameters in the EOS	a, b, c
The smallest diameter of deforming bubble and droplet	B
Lattice speed	c
Capillary number	Ca
Lattice speed of sound	c_s
A parameter for determining the amount of bubble (droplet) deformation	D
Second-order isotropy coefficient	e_2
Fourth-order isotropy coefficient	e_4
Lattice velocity vectors	e_i
Particle probability distribution function	f_i
Equilibrium distribution function	f_i^{eq}
Discrete form of intermolecular body force	F_i
The nth part of the intermolecular force term	$F^{(n)}$
Inter-particle interaction strength	G
Distance between two parallel plates	H
Inverse of the capillary number	k
The largest diameter of deforming bubble (droplet)	L
Parameters related to pseudo-potential functions	L_j, E_j, H_j
A parameter used in surface tension	M_j
Pressure	p
Saturation pressure	p_0
Critical pressure	p_c
First component of the pressure tensor	p_{xx}
Radius of the bubble or droplet before deformation	r
Ideal gas constant	R
A free parameter used in P_{xx}	s_j

Time	t
Temperature	T
Critical temperature	T_c
Reduced temperature	T_r
Microscopic velocity	$\overrightarrow{u}$
Velocity components of the northern moving wall	u_N, v_N
The αth component of macroscopic velocity	u_α
The αth component of equilibrium velocity	u_α^{eq}
Location vector	x
A parameter which is calculated by a, b, and c	$Z = bc^2/a$
A variable defined in EOS	α
Shear rate	$\dot{\gamma}$
Angle between the principal axis of the bubble (longest dimension) and the wall direction	θ
Viscosity ratio	λ
Dynamic viscosity	μ
Kinematic viscosity	ν
Density	ρ
Critical density	ρ_c
Reduced density	ρ_R
Surface tension	σ
Relaxation time	τ
Pseudo-potential function	ψ
Acentric factor	ω
Weighting coefficients	ω_i
Interface layer thickness	Γ
BGK	Bhatnagar Gross and Krook
C-S	Carnahan-Starling
EOS	Equation of state
LBM	Lattice Boltzmann method
P-R	Peng-Robinson
SC	Shan-Chen
SRK	Soave-Redlich-Kwong
VdW	Van der Waals

References

[1] Q. LI ET AL., *An improved single-relaxation-time multiphase lattice Boltzmann model for multiphase flows with large density ratios and high Reynolds numbers,* Adv. Appl. Math. Mech., (13) (2021), pp. 426–454.

[2] Z. GUO, ET AL., *A diffuse domain method for two-phase flows with large density ratio in complex geometries,* J. Fluid Mech., 907 (2021).

[3] V. DUKE-WALKER, ET AL., *Evaporation and breakup effects in the shock-driven multiphase instability,* J. Fluid Mech., 908 (2021).

[4] C. HARWOOD, ET AL., *The hydroelastic response of a surface-piercing hydrofoil in multiphase flows. Part 2. Modal parameters and generalized fluid forces,* J. Fluid Mech., 884 (2020).

[5] G. HÁZI, ET AL., *Lattice Boltzmann methods for two-phase flow modeling,* Ann. Nuclear Energy, 29(12) (2002), pp. 1421–1453.

[6] T. INAMURO, ET AL., *A lattice Boltzmann method for incompressible two-phase flows with large density differences,* J. Comput. Phys., 198(2) (2004), pp. 628–644.

[7] K. SANKARANARAYANAN, ET AL., *A comparative study of lattice Boltzmann and front-tracking finite-difference methods for bubble simulations,* Int. J. Multiphase Flow, 29(1) (2003), pp. 109–116.

[8] H. LIU, A.J. VALOCCHI, AND Q. KANG, *Three-dimensional lattice Boltzmann model for immiscible two-phase flow simulations,* Phys. Rev. E, 85(4) (2012), 046309.

[9] L.-S. LUO, *Unified theory of lattice Boltzmann models for nonideal gases,* Phys. Rev. Lett., 81(8) (1998), p. 1618.

[10] R. SCARDOVELLI, AND S. ZALESKI, *Direct numerical simulation of free-surface and interfacial flow,* Ann. Rev. Fluid Mech., 31(1) (1999), pp. 567–603.

[11] A. K. GUNSTENSEN, ET AL., *Lattice Boltzmann model of immiscible fluids,* Phys. Rev. A, 43(8) (1991), p. 4320.

[12] X. SHAN, AND H. CHEN, *Lattice Boltzmann model for simulating flows with multiple phases and components,* Phys. Rev. E, 47(3) (1993), p. 1815.

[13] X. SHAN, AND H. CHEN, *Simulation of nonideal gases and liquid-gas phase transitions by the lattice Boltzmann equation,* PPhys. Rev. E, 49(4) (1994), p. 2941.

[14] M. SWIFT, W. OSBORN, *and J. Yeomans, Lattice Boltzmann simulation of nonideal fluids,* Phys. Rev. Lett., 75(5) (1995), p. 830.

[15] M. SWIFT, ET AL., *Lattice Boltzmann simulations of liquid-gas and binary fluid systems,* Phys. Rev. E, 54(5) (1995), p. 5041.

[16] S. SUCCI, The Lattice Boltzmann Equation: for Fluid Dynamics and Beyond, Oxford University Press, 2001.

[17] S. KHAJEPOR, AND B. CHEN, *Multipseudopotential interaction: A consistent study of cubic equations of state in lattice Boltzmann models,* Phys. Rev. E, 93(1) (2016), 013303.

[18] R. BENZI, ET AL., *Mesoscopic modeling of a two-phase flow in the presence of boundaries: the contact angle,* Phys. Rev. E, 74(2) (2006), 021509.

[19] M. SBRAGAGLIA, ET AL., *Generalized lattice Boltzmann method with multirange pseudopotential,* Phys. Rev. E, 75(2) (2007), 026702.

[20] X. HE, AND G. DOOLEN, *Thermodynamic foundations of kinetic theory and lattice Boltzmann models for multiphase flows,* J. Stat. Phys., 107(1-2) (2002), pp. 309–328.

[21] X. SHAN, *Pressure tensor calculation in a class of nonideal gas lattice Boltzmann models,* Phys. Rev. E, 77(6) (2008), 066702.

[22] M. SBRAGAGLIA, ET AL., *Lattice Boltzmann method with self-consistent thermo-hydrodynamic*

equilibria, J. Fluid Mech., 628 (2009), pp. 299–309.

[23] M. SBRAGAGLIA, AND X. SHAN, *Consistent pseudopotential interactions in lattice Boltzmann models,* Phys. Rev. E, 84(3) (2011), 036703.

[24] A. GUPTA, AND R. KUMAR, *Lattice Boltzmann simulation to study multiple bubble dynamics,* Int. J. Heat Mass Transfer, 51 (2008), pp. 5192–5203.

[25] Z. YU, AND L.-S. FAN, *Multirelaxation-time interaction-potential-based lattice Boltzmann model for two-phase flow,* Phys. Rev. E, 82(4) (2010), 046708.

[26] Q. LI, K. H. LUO, AND X. LI, *Forcing scheme in pseudopotential lattice Boltzmann model for multiphase flows,* Phys. Rev. E, 86(1) (2012), 016709.

[27] G. TAYLOR, *The formation of emulsions in definable fields of flow,* Proceedings of the Royal Society of London. Series A, Containing Papers of a Mathematical and Physical Character, 146(858) (1934), pp. 501–523.

[28] C. CHAFFEY, AND H. BRENNER, *A second-order theory for shear deformation of drops,* J. Colloid Interface Sci., 24(2) (1967), pp. 258–269.

[29] R. COX, *The deformation of a drop in a general time-dependent fluid flow,* J. Fluid Mech., 37(3) (1969), pp. 601–623.

[30] H. GRACE, *Dispersion phenomena in high viscosity immiscible fluid systems and application of static mixers as dispersion devices in such systems,* Chem. Eng. Commun., 14(3-6) (1982), pp. 225–277.

[31] S. TORZA, R. COX, AND S. MASON, *Particle motions in sheared suspensions XXVII. Transient and steady deformation and burst of liquid drops,* J. Colloid Interface Sci., 38(2) (1972), pp. 395–411.

[32] E. HINCH, AND A. ACRIVOS, *Steady long slender droplets in two-dimensional straining motion,* J. Fluid Mech., 91(3) (1979), p. 401.

[33] E. HINCH, AND A. ACRIVOS, *Long slender drops in a simple shear flow,* J. Fluid Mech., 98(2) (1980), pp. 305–328.

[34] J. RALLISON, *Note on the time-dependent deformation of a viscous drop which is almost spherical,* J. Fluid Mech., 98(3) (1980), pp. 625–633.

[35] J. RALLISON, *A numerical study of the deformation and burst of a viscous drop in general shear flows,* J. Fluid Mech., 109 (1981), pp. 465–482.

[36] J. RALLISON, *The deformation of small viscous drops and bubbles in shear flows,* Ann. Rev. Fluid Mech., 16(1) (1984), pp. 45–66.

[37] B. BENTLEY, AND L. G. LEAL, *An experimental investigation of drop deformation and breakup in steady, two-dimensional linear flows,* J. Fluid Mech., 167 (1986), pp. 241–283.

[38] E. CANEDO, ET AL., *An experimental study of bubble deformation in viscous liquids in simple shear flow,* AIChE J., 39(4) (1993), pp. 553–559.

[39] P. MAFFETTONE, AND M. MINALE, *Equation of change for ellipsoidal drops in viscous flow,* J. Non-Newtonian Fluid Mech., 78(2-3) (1998), pp. 227–241.

[40] A. RUST, AND M. MANGA, *Bubble shapes and orientations in low Re simple shear flow,* J. Colloid Interface Sci., 249(2) (2002), pp. 476–480.

[41] N. MÜLLER-FISCHER, ET AL., *Single bubble deformation and breakup in simple shear flow,* Exp. Fluids, 45(5) (2008), pp. 917–926.

[42] A. KOMRAKOVA, ET AL., *Lattice Boltzmann simulations of drop deformation and breakup in shear flow,* Int. J. Multiphase Flow, 59 (2014), pp. 24–43.

[43] D. ANDERL, ET AL., *Numerical simulation of bubbles in shear flow,* PAMM, 14(1) (2014), pp. 667–668.

[44] Y.-H. QIAN, D. D'HUMIÈRES, AND P. LALLEMAND, *Lattice BGK models for Navier-Stokes equa-*

tion, Europhys. Lett., 17(6) (1992), p. 479.

[45] K. SUN, ET AL., *Evaluation of force implementation in pseudopotential-based multiphase lattice Boltzmann models,* Physica A: Statistical Mechanics and Its Applications, 391(15) (2012), pp. 3895–3907.

[46] S. KHAJEPOR, J. WEN, AND B. CHEN, *Multipseudopotential interaction: A solution for thermodynamic inconsistency in pseudopotential lattice Boltzmann models,* Phys. Rev. E, 91(2) (2015), 023301.

[47] X. SHAN, *Analysis and reduction of the spurious current in a class of multiphase lattice Boltzmann models,* Phys. Rev. E, 73(4) (2006), 047701.

[48] U. FRISCH, B. HASSLACHER, AND Y. POMEAU, *Lattice-gas automata for the Navier-Stokes equation,* Phys. Rev. Lett., 56(14) (1986), p. 1505.

[49] X. HE, AND L.-S. LUO, *Theory of the lattice Boltzmann method: From the Boltzmann equation to the lattice Boltzmann equation,* Phys. Rev. E, 56(6) (1997), p. 6811.

[50] A. LADD, AND R. VERBERG, *Lattice-Boltzmann simulations of particle-fluid suspensions,* J. Stat. Phys., 104(5-6) (2001), pp. 1191–1251.

[51] A. KUPERSHTOKH, AND D. MEDVEDEV, *Lattice Boltzmann equation method in electrohydrodynamic problems,* J. Electrostatics, 64(7-9) (2006), pp. 581–585.

[52] N. MARTYS, X. SHAN, AND H. CHEN, *Evaluation of the external force term in the discrete Boltzmann equation,* Phys. Rev. E, 58(5) (1998), p. 6855.

[53] Z. GUO, C. ZHENG, AND B. SHI, *Discrete lattice effects on the forcing term in the lattice Boltzmann method,* Phys. Rev. E, 65(4) (2002), 046308.

[54] Q. ZOU, AND X. HE, *On pressure and velocity boundary conditions for the lattice Boltzmann BGK model,* Phys. Fluids, 9(6) (1997), pp. 1591–1598.

[55] W. BARTOK, W. AND S. MASON, *Particle motions in sheared suspensions: VIII. Singlets and doublets of fluid spheres,* J. Colloid Sci., 14(1) (1959), pp. 13–26.

[56] F. RUMSCHEIDT, AND S. MASON, *Particle motions in sheared suspensions XII. Deformation and burst of fluid drops in shear and hyperbolic flow,* J. Colloid Sci., 16(3) (1961), pp. 238–261.

[57] G. TAYLOR, *The viscosity of a fluid containing small drops of another fluid,* Proceedings of the Royal Society of London, Series A, Containing Papers of a Mathematical and Physical Character, 138(834) (1932), pp. 41–48.

[58] F. HAKIMI, AND W. SCHOWALTER, *The effects of shear and vorticity on deformation of a drop,* J. Fluid Mech., 98(3) (1980), pp. 635–645.

[59] G. YOUNGREN, AND A. ACRIVOS, *On the shape of a gas bubble in a viscous extensional flow,* J. Fluid Mech., 76(3) (1976), pp. 433–442.

[60] A. ACRIVOS, AND T. LO, *Deformation and breakup of a single slender drop in an extensional flow,* J. Fluid Mech., 86(4) (1978), pp. 641–672.

[61] J. EVANS, *Dimensional analysis and the Buckingham pi theorem,* American J. Phys., 40(12) (1972), pp. 1815–1822.

[62] A. WAGNER, *Thermodynamic consistency of liquid-gas lattice Boltzmann simulations,* Phys. Rev. E, 74(5) (2006), 056703.

[63] M. NGACHIN, ET AL., *Lattice Boltzmann simulation of rising bubble dynamics using an effective buoyancy method,* Int. J. Modern Phys. C, 26(03) (2015), 1550031.